JACS
JOURNAL OF THE AMERICAN CHEMICAL SOCIETY

Article

pubs.acs.org/JACS

Visualization of Peroxynitrite-Induced Changes of Labile Zn^{2+} in the Endoplasmic Reticulum with Benzoresorufin-Based Fluorescent Probes

Wei Lin,[‡] Daniela Buccella,[‡,†] and Stephen J. Lippard*[,‡]

[‡]Department of Chemistry, Massachusetts Institute of Technology, Cambridge, Massachusetts 02139, United States

[†]Department of Chemistry, New York University, New York, New York 10003, United States

Supporting Information

ABSTRACT: Zn^{2+} plays essential roles in biology, and the homeostasis of Zn^{2+} is tightly regulated in all cells. Subcellular distribution and trafficking of labile Zn^{2+}, and its inter-relation with reactive nitrogen species, are poorly understood due to the scarcity of appropriate imaging tools. We report a new family of red-emitting fluorescent sensors for labile Zn^{2+}, ZBR1−3, based on a benzoresorufin platform functionalized with dipicolylamine or picolylamine-derived metal binding groups. In combination, the pendant amines and fluorophore afford an $[N_3O]$ binding motif that resembles that of previously reported fluorescein-based sensors of the Zinpyr family, reproducing well their binding capabilities and yielding comparable K_d values in the sub-nanomolar and picomolar ranges. The ZBR sensors display up to 8.4-fold emission fluorescence enhancement upon Zn^{2+} binding in the cuvette, with similar responses obtained in live cells using standard wide-field fluorescence microscopy imaging. The new sensors localize spontaneously in the endoplasmic reticulum (ER) of various tested cell lines, allowing for organelle-specific monitoring of zinc levels in live cells. Study of ER zinc levels in neural stem cells treated with a peroxynitrite generator, Sin-1, revealed an immediate decrease in labile Zn^{2+} thus providing evidence for a direct connection between ER stress and ER Zn^{2+} homeostasis.

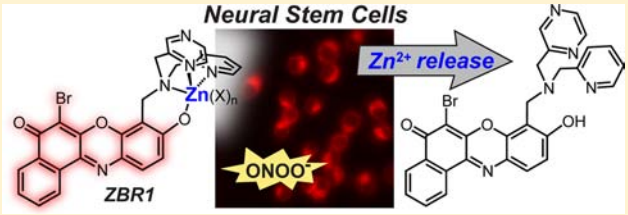

INTRODUCTION

Zinc is a d-block element essential for all living organisms.[1,2] Zn^{2+} ions play various key roles in biological systems including enzymatic catalysis, stabilization of protein structure, and modulation of interactions between macromolecules.[3] The percentage of genes coding for zinc-bound proteins is estimated to be 10%, consistent with the value found in the known proteome.[4,5] The total concentration of Zn^{2+} in mammalian cells is estimated to be in the range of 100 to 500 μM;[6] the largest fraction is tightly bound to metalloproteins, whereas a smaller portion is loosely bound to various readily exchangeable molecules.[7] Cytosolic pools of labile Zn^{2+} participate in signaling pathways associated with different physiological and pathological events.[8−10] The intracellular sources of these pools of exchangeable zinc, however, remain unclear in many systems.

Zinc and reactive nitrogen species (RNS) such as nitric oxide (NO) and peroxynitrite ($ONOO^-$) have physiological roles in the nervous system and are implicated in neurological dysfunction.[11−13] Exposure of neurons to high concentrations of exogenous NO leads to the formation of peroxynitrite and causes Zn^{2+} release from intracellular stores. In turn, higher concentrations of labile Zn^{2+} induce mitochondrial dysfunction and increased production of reactive oxygen species (ROS), thus resulting in amplification of the apoptotic signaling pathway contributing to neurodegeneration.[12] High concentrations of NO and peroxynitrite also have an effect on the endoplasmic reticulum (ER), inducing ER stress and activating a cellular stress response named unfolded protein response (UPR).[14,15] A number of neurodegenerative disorders such as Alzheimer's disease, Parkinson's disease, prion disease, Huntington's disease, frontotemporal dementia, amyotrophic lateral sclerosis, and Ehlers−Danlos syndrome are all characterized by the accumulation and aggregation of misfolded proteins in the ER.[16,17] Previous studies demonstrated that deletion of zinc transporters and zinc deficiency in the ER up-regulates the UPR.[18,19]

The temporal, spatial, and functional characteristics of the interplay between RNS, ROS, and labile Zn^{2+} in neurodegeneration are still far from clear. New approaches are needed to track the source and destination of these species in live cells and tissues. In particular, convenient tools that allow for easy visualization of the fluctuations of labile Zn^{2+} in specific organelles and its translocation to or from the cytosol may shed some light on the role of Zn^{2+} in these pathologies. Neural stem cells (NSCs) are a class of cells that can proliferate through symmetric division and differentiate into neurons and glial cells through asymmetric division.[20] Owing to their ability to self-renew and produce neurons and glial cells, NSCs are a powerful resource to study synaptic plasticity and neuronal disorders.[21−26] In this work we employ NSCs to investigate the

Received: June 13, 2013
Published: July 31, 2013

   dx.doi.org/10.1021/ja4059487 | J. Am. Chem. Soc. 2013, 135, 13512−13520

inter-relation between RNS and zinc homeostasis with potential implications for understanding neurodegenerative processes.

Over the past decade, our group has developed a large number of fluorescein-based fluorescent sensors for mobile zinc with apparent dissociation constants spanning the range from sub-nanomolar to sub-millimolar.[27] Among these, the Zinpyr[28] (ZP) family is a series of probes containing dipicolylamine (DPA) or DPA-analogue metal binding moieties with dissociation constants in the nanomolar range,[27,29,30] which have proved to be particularly useful for the imaging of Zn^{2+} distribution, uptake, and translocation in different types of cells.[31−34] Fluorescein-based sensors, however, are limited by their high energy absorptions and small Stokes shifts. Cellular auto-fluorescence in the corresponding spectral window leads to a high background signal that reduces the distinguishable fluorescence turn-on of probes associated with Zn^{2+} binding, compared to the response obtained in the cuvette. For biological imaging, sensors emitting in the red or near-infrared region are thus desirable.

In our continuing efforts to improve the tools available for the study of labile Zn^{2+} in memory formation, neurodegeneration, and sensory perception, we herein report the design of a new series of probes based on a benzoresorufin fluorophore with a DPA or DPA-analogue metal binding group. The resulting red-emitting probes display a conserved $[N_3O]$ zinc-binding motif similar to that offered by ZP analogues (Figure 1), which endows them with dissociation constants

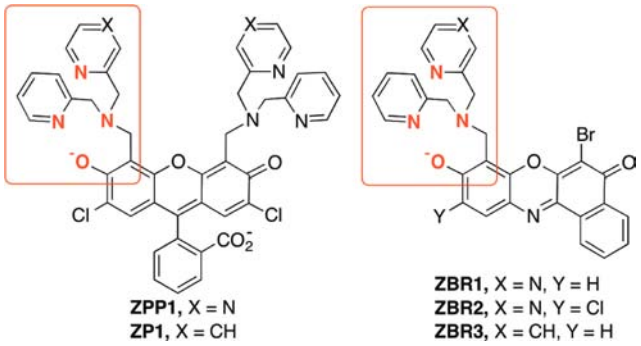

Figure 1. General structures of ZP and ZBR zinc sensor families.

similar to those of their green-emitting counterparts. We employed the new probes to study zinc homeostasis in NSCs and demonstrate that the peroxynitrite generator Sin-1 can modulate labile Zn^{2+} in the ER. We thus provide direct evidence of the interplay between RNS-induced ER stress and Zn^{2+} signaling.

MATERIALS AND METHODS

Synthetic Materials and Methods. All synthetic procedures were performed under a nitrogen atmosphere unless otherwise specified. 4-Chloro-2-methylresorcinol,[35] 6-bromo-8-(bromomethyl)-5-oxo-benzo[*a*]phenoxazin-9-yl acetate,[36] and (2-picolyl)(pyrazin-2-yl-methyl)amine[33] were synthesized according to reported procedures. All other reagents were purchased from commercial sources and used as received. Solvents were purified and degassed by standard procedures. NMR spectra were acquired on Bruker Avance 400 spectrometers. ^{1}H NMR chemical shifts are reported in ppm relative to $SiMe_4$ (δ = 0) and were referenced internally with respect to residual protons in the solvent (δ = 7.26 for $CHCl_3$, 3.31 for CD_2HOD, 2.50 for DMSO-d_5). ^{13}C NMR chemical shifts are reported in ppm relative to $SiMe_4$ (δ = 0) and were referenced internally with respect to the solvent signal (δ = 77.16 for $CDCl_3$, 49.00 for CD_3OD, 39.52 for DMSO-d_6). Low-resolution mass spectra were acquired on an Agilent 1100 series LC/MSD trap spectrometer, using electrospray ionization. High-resolution mass spectrometry (HRMS) was conducted by staff at the MIT Department of Chemistry Instrumentation Facility on a Bruker Daltonics APEXIV 4.7 T FT-ICR-MS instrument.

Synthesis of 4-Chloro-6-nitroso-2-methylresorcinol, 1b. A solution of 4-chloro-2-methylresorcinol (2.00 g, 12.6 mmol) in ethanol (12.5 mL) was cooled to 0 °C and treated with a solution of KOH (0.991 g, 17.6 mmol) in water (4.2 mL), followed by isoamyl nitrite (2.0 mL, 15 mmol) added dropwise. After addition was complete, the solution was allowed to warm to room temperature and stirred for 1.5 h. The mixture was acidified to pH ∼2 by addition of 1 M HCl, and stirring was continued at room temperature, open to air, for 1 h. The yellow precipitate was collected by filtration, washed with a 1:1 mixture of ethanol:water (2 × 10 mL), followed by water (30 mL), and dried under vacuum to give 4-chloro-6-nitroso-2-methylresorcinol as a bright yellow powder (1.95 g, 82%). ^{1}H NMR (400 MHz, MeOH-d_4, room temperature): δ 7.70 (s, 1H), 1.89 (s, 3H). ^{13}C{^{1}H} NMR (100.6 MHz, MeOH-d_4): δ 181.8, 158.5, 144.8, 137.8, 119.3, 115.2, 8.4. ESI-MS (m/z): $[M+H^+]$ calcd for $C_7H_6ClNO_3$, 188.0; found, 188.1.

Synthesis of 10-Chloro-9-hydroxy-8-methyl-5-benzo[*a*]-phenoxazone, 2b. A suspension of 4-chloro-6-nitroso-2-methyl-resorcinol (0.750 g, 4.00 mmol) in *n*-butanol (7.5 mL) was mixed with a solution of 1,3-dihydroxynaphthalene (0.640 g, 4.00 mmol) in *n*-butanol (7.5 mL) and heated to 50 °C. Concentrated sulfuric acid (1.5 mL) was added dropwise to the warm reaction mixture, open to air, and heating was continued for an additional 1 h. The suspension was then allowed to stand at room temperature overnight. The solid was collected by centrifugation, and the pellet was washed with a 1:1 mixture of ethanol:*n*-butanol (2 × 10 mL), followed by 1:1 ethanol:water (5 mL), and dried under vacuum to give resorufin **2b** as a brown-red powder (1.03 g, 80% yield). The crude product was used in the next step without further purification.

Synthesis of 10-Chloro-8-methyl-5-oxo-benzo[*a*]-phenoxazin-9-yl Acetate, 3b. A suspension of 10-chloro-9-hydroxy-8-methyl-5-benzo[*a*]phenoxazone, **2b** (1.00 g, 3.21 mmol), in acetic anhydride (13 mL) was treated with pyridine (1.3 mL) and heated to 100 °C for 3 h with vigorous stirring. The resulting suspension was allowed to stand at room temperature for 12 h. The solid was collected by filtration, washed with fresh acetic anhydride (5 mL), followed by water (2 × 5 mL), and dried under vacuum to give the acetate product as an orange-yellow solid (1.01 g, 89%). ^{1}H NMR (400 MHz, $CDCl_3$, room temperature): δ 8.57 (m, 1H), 8.22 (m, 1H), 7.72 (m, 2H), 7.68 (s, 1H), 6.38 (s, 1H), 2.42 (s, 3H), 2.25 (s, 3H). ^{13}C{^{1}H} NMR (100.6 MHz, $CDCl_3$): δ 183.7, 167.8, 150.6, 147.7, 147.4, 141.3, 132.3, 132.3, 131.0, 130.9, 127.4, 126.0, 124.9, 123.7, 120.8, 108.0, 20.4, 9.5. ESI-MS (m/z): $[M+H^+]$ calcd for $C_{19}H_{12}ClNO_4$, 354.1; found, 354.0.

Synthesis of 6-Bromo-8-(bromomethyl)-10-chloro-5-oxo-benzo[*a*]phenoxazin-9-yl Acetate, 4b. A mixture of benzo-resorufin acetate **3b** (800 mg, 2.26 mmol) and 1,3-dibromo-5,5-dimethylhydantoin (1.426 g, 4.98 mmol) in chlorobenzene (90 mL) was treated with Vazo 88 (184 mg, 0.746 mmol) and acetic acid (100 mL) and heated to 50 °C for 48 h, after which abundant precipitate of the ring-brominated intermediate was observed. The suspension was then heated to 60 °C to aid in re-dissolving the intermediate, and aliquots were monitored by ^{1}H NMR until reaction completion (1−4 more days). The reaction mixture was washed with water at 60 °C (3 × 100 mL) and once with brine, and then it was dried over Na_2SO_4 and evaporated to an orange solid (1.021 g, 88%). ^{1}H NMR (400 MHz, $CDCl_3$, room temperature): δ 8.67 (d, ^3J = 7 Hz, 1H), 8.36 (d, ^3J = 7 Hz, 1H), 7.93 (s, 1H), 7.82 (t, ^3J = 7 Hz, 1H), 7.80 (t, ^3J = 7 Hz, 1H), 4.67 (s, 2H), 2.50 (s, 3H). ^{13}C{^{1}H} NMR (100.6 MHz, $CDCl_3$): 177.4, 167.3, 147.7, 147.6, 147.2, 140.9, 132.9, 132.8, 131.4, 131.3, 130.0, 127.2, 125.3, 125.2, 121.0, 34.0, 20.6. ESI-MS (m/z): $[M+H^+]$ calcd for $C_{19}H_{10}Br_2ClNO_4$, 511.9; found, 511.8.

Synthesis of ZBR1. A mixture of bromomethyl benzophenoxazone **4a** (150 mg, 0.314 mmol), (2-picolyl)(pyrazin-2-yl-methyl)amine (190 mg, 0.949 mmol), and potassium carbonate (435 mg, 3.14 mmol) in

dx.doi.org/10.1021/ja4059487 | J. Am. Chem. Soc. 2013, 135, 13512−13520

acetonitrile (6 mL) was heated to reflux for 3 h. The mixture was allowed to cool to room temperature and diluted with saturated NH_4Cl and dichloromethane in equal amounts. The organic phase was separated and washed once more with NH_4Cl, three times with water, and once with brine, and then it was dried over Na_2SO_4 and evaporated. The residue was triturated with 1:1 Et_2O/pentane to give ZBR1 as a red-brown powder (108.4 mg, 62%). The product may be recrystallized by slow diffusion of 1:1 Et_2O/pentane into a dichloromethane solution of the compound to yield ZBR1·CH_2Cl_2. ^{1}H NMR (400 MHz, $CDCl_3$, room temperature): δ 8.69 (d, ^3J = 7 Hz, 1H), 8.64 (m, 2H), 8.48 (s, 1H), 8.43 (d, ^4J = 2 Hz, 1H), 8.38 (d, ^3J = 7 Hz, 1H), 7.78 (t, ^3J = 7 Hz, 1H), 7.74−7.69 (m, 3H), 7.27 (m, overlapping solvent), 7.03 (d, ^3J = 8 Hz, 1H), 4.25 (s, 2H), 4.05 (s, 4H). $^{13}C\{^1H\}$ NMR (100.6 MHz, $CDCl_3$) δ 177.5, 162.8, 156.9, 153.9, 148.8, 148.7, 145.5, 143.8, 143.62, 143.56, 141.5, 137.5, 132.2, 131.2, 130.8, 130.6, 126.8, 126.5, 124.5, 133.4, 122.9, 116.1, 110.0, 105.7, 58.4, 57.3, 47.8. ESI-HRMS (m/z): [M+H$^+$] calcd for $C_{28}H_{20}BrN_5O_3$, 556.0822; found, 556.0808. Anal. Calcd for $C_{28}H_{19}BrN_5O_3$: C, 60.66; H, 3.64; N, 12.63. Found: C, 60.60; H, 3.78; N, 12.43.

Synthesis of ZBR2. A mixture of bromomethyl benzophenoxazone **4b** (150 mg, 0.293 mmol), (2-picolyl)(pyrazin-2-yl-methyl)amine (177 mg, 0.884 mmol), and potassium carbonate (405 mg, 2.93 mmol) in acetonitrile (6 mL) was heated to reflux for 3 h. The mixture was allowed to cool to room temperature and diluted with saturated NH_4Cl and dichloromethane in equal amounts. The organic phase was separated and washed once more with NH_4Cl, three times with water, once with brine, and then it was dried over Na_2SO_4 and evaporated. The residue was triturated with 1:1 Et_2O/pentane to give ZBR2 as a red-brown powder (88.0 mg, 51%). The product may be recrystallized by slow liquid diffusion of 1:1 Et_2O/pentane into a dichloromethane solution of the compound. ^{1}H NMR (400 MHz, $CDCl_3$, room temperature): δ 8.70 (d, ^3J = 5 Hz, 1H), 8.65 (m, 2H), 8.49 (s, 1H), 8.44 (s, 1H), 8.36 (d, ^3J = 8 Hz, 1H), 7.84 (s, 1H), 7.79−7.69 (m, 3H), 7.31−7.26 (m, overlapping solvent), 4.26 (s, 2H), 4.04 (s, 4H). $^{13}C\{^1H\}$ NMR (100.6 MHz, $CDCl_3$) δ 177.4, 158.2, 156.5, 153.7, 148.7, 148.5, 145.4, 143.8, 143.7, 142.7, 142.1, 137.8, 132.4, 131.6, 131.2, 130.6, 129.8, 126.9, 126.1, 124.7, 123.5, 123.0, 120.3, 111.1, 106.3, 58.0, 57.3, 48.0. ESI-HRMS (m/z): [M+H$^+$] calcd for $C_{28}H_{19}BrClN_5O_3$, 590.0424; found, 590.0413.

Synthesis of ZBR3. A mixture of bromomethyl benzophenoxazone **4a** (150.0 mg, 0.314 mmol), di(2-picolyl)amine (190 mg, 0.954 mmol), and potassium carbonate (435.0 mg, 3.14 mmol) in acetonitrile (6 mL) was heated to reflux for 3 h. The mixture was allowed to cool to room temperature and diluted with equal volumes of saturated NH_4Cl and dichloromethane (50 mL each). The organic phase was separated and washed once more with NH_4Cl, three times with water, and once with brine, and then it was dried over Na_2SO_4 and evaporated. The residue was triturated with 1:1 Et_2O/pentane to give ZBR3 as a red-brown powder (96.1 mg, 55%). The product may be recrystallized by slow liquid diffusion (layering) of 1:1 Et_2O/pentane into a dichloromethane solution of the compound to yield red-brown needles. ^{1}H NMR (400 MHz, $CDCl_3$, room temperature): δ 8.70 (d, ^3J = 5 Hz, 1H), 8.65 (m, 2H), 8.49 (s, 1H), 8.44 (s, 1H), 8.36 (d, ^3J = 8 Hz, 1H), 7.84 (s, 1H), 7.79−7.69 (m, 3H), 7.31−7.26 (m, overlapping solvent), 4.26 (s, 2H), 4.04 (s, 4H). $^{13}C\{^1H\}$ NMR (100.6 MHz, $CDCl_3$) δ 177.4, 158.2, 156.5, 153.7, 148.7, 148.5, 145.4, 143.8, 143.7, 142.7, 142.1, 137.8, 132.4, 131.6, 131.2, 130.6, 129.8, 126.9, 126.1, 124.7, 123.5, 123.0, 120.3, 111.1, 106.3, 58.0, 57.3, 48.0. HRMS (m/z): [M−H$^+$] calcd for $C_{29}H_{21}BrN_4O_3$, 551.0724; found, 551.0719.

Spectroscopic Methods. All aqueous solutions were prepared with deionized H_2O (Millipore). Other solvents were supplied by Aldrich. Piperazine-*N*,*N*′-bis(2-ethanesulfonic acid) (PIPES) and 99.999% KCl were purchased from Calbiochem. High-purity 25% HCl, 45% KOH, 50% NaOH, and 99.999% $ZnCl_2$ were supplied by Aldrich. Stock solutions of ZBR sensors in dimethyl sulfoxide (DMSO) were prepared in the 0.5−1.0 mM range, stored at −20 °C in 100−200 μL aliquots, and thawed immediately before each experiment. All spectroscopic measurements were conducted in aqueous buffer containing 50 mM PIPES (pH 7.0) and 100 mM KCl except the pK_a titrations. The buffer solutions were pretreated with Chelex resin (Bio-Rad) to remove residual metal ion in solution. The pH measurements were made using a Mettler Toledo FE20 pH meter. UV−visible spectra were acquired on a Cary 1E spectrophotometer using quartz cuvettes (1 cm path length). Fluorescence spectra were acquired on a QuantaMaster 4 Photon Technology International fluorometer. All measurements were conducted at 25.0 °C, maintained by a circulating water bath. Extinction coefficients were determined in the 1−10 μM range in buffer solutions at pH 7.0 with the presence of 10 μM EDTA for the metal-free form or with 20 μM $ZnCl_2$ for the metal-bound form of the sensor. Fluorescence quantum yields were determined using 1−5 μM sensor in buffer solution at pH 7.0, exciting at the excitation maximum of the corresponding sensor. Due to poor solubility in aqueous solution, the extinction coefficients and quantum yield of ZBR3 were obtained in the 0.4−2 μM range. The quantum yield calculation was standardized to resorufin, with a reported quantum yield of 0.74 at pH 9.5 at 572 nm excitation.[37] Fluorescence emission spectra were integrated from 550 to 800 nm.

Cell Cultures and Staining Procedures. HeLa and macrophage 246.7 cells were incubated in Dulbecco's Modified Eagle Medium (DMEM, GIBCO), supplemented with 10% heat-deactivated fetal bovine serum (FBS) and 1% penicillin/streptomycin, at 37 °C in a humidified atmosphere with 5% CO_2. NSCs were originally isolated from the hippocampus of adult rats as previously described,[38,39] and they were maintained in DMEM/F12 medium (GIBCO) with 20 ng/mL FGF2 (Pepro Tech) and N-2 supplement (GIBCO) at 37 °C in a humidified atmosphere with 5% CO_2. Cells were plated in 35 mm glass-bottom culture dishes with 14 mm opening (MatTek) 24−48 h before imaging. All the cells used were at the passage number from 5 to 15, and experiments were repeated using a minimum of two separate frozen cell stocks. A confluence level of 50−70% was reached at imaging. Cells were incubated with sensors at 37 °C for 30 min before mounting to the microscope. The growth medium was replaced with fresh DMEM containing 5 μM sensor (from a 1 mM stock solution in DMSO) before imaging. The organelle-specific dyes Hoechst 33258 (Aldrich, final concentration 5 μM), MitoTracker Green (Invitrogen, final concentration 0.1−0.5 μM), and ER-Tracker Blue-White DPX (Invitrogen, final concentration 1−5 μM) were incubated for 30 min before imaging. Golgi-specific staining BacMam 2.0 (Invitrogen, final concentration 10 particles per cell) was incubated for 24 h to transduce the cells. Cells were rinsed with sterile PBS buffer (2 × 2 mL) and then with dye-free DMEM without serum (2 mL) to remove excess unbound sensors. Cells were bathed in 2 mL of dye-free DMEM without serum before mounting on the microscope. To measure Zn^{2+}-induced fluorescence changes, cells were treated with 25 μM $ZnCl_2$ and 50 μM sodium pyrithione (2-pyridinethiol-1-oxide) in DMSO. A portion of 100 μM *N*,*N*,*N*′,*N*′-tetrakis(2-pyridylmethyl)-ethylenediamine (TPEN) or tris(2-pyridylmethyl)amine (TPA) was applied to the Petri dish to reverse the fluorescence response induced by zinc. For experiments involving Sin-1, a 10 mM working solution of the reagent (Sigma) was freshly prepared by dissolving solid Sin-1 in 1× phosphate-buffered saline (PBS) (Corning Cellgro). After initial images were acquired, 20 μL of the Sin-1 working solution was applied to the Petri dish containing 2 mL of dye-free DMEM/F12 medium to obtain a final concentration of 100 μM.

Fluorescence Microscopy. Fluorescence imaging experiments were performed using a Zeiss Axiovert 200M inverted epifluorescence microscope with a Hamamatsu EM-CCD digital camera C9100 and a MS200 XY Piezo Z stage (Applied Scientific Instruments, Inc.). An X-Cite 120 metal halide lamp (EXFO) was used as the light source. Zeiss standard filter sets 49, 38 HE, and 43 HE were employed for imaging Hoechst 33258/ER-Tracker, MitoTracker Green/BacMam 2.0 Golgi staining, and ZBR sensors. The microscope was operated with Volocity software (version 6.01, Improvision). The exposure time for acquisition of fluorescence images was kept constant for each series of images at each channel. Images corresponding to co-localization studies were deconvoluted using Volocity restoration algorithms. The Pearson's correlation values were obtained in Volocity to evaluate the co-localization level of ZBR sensors with specific organelle trackers. Z-

sectioned images were obtained at 0.3 μm intervals in a 20 μm range to discern possible effects of organelle fluorescence overlap along the *Z*-axis. The quantification of fluorescence intensity was analyzed using ImageJ (version 1.45, NIH). The whole cell was selected as region of interest. The integrated fluorescence from the background region was subtracted from the integrated fluorescence intensity of the cell body region. The relative change of fluorescence intensity was plotted for comparison.

$$\text{Pearson's Correlation} = \frac{\sum_i (x_i - x_{\text{aver}})(y_i - y_{\text{aver}})}{\sqrt{\sum_i (x_i - x_{\text{aver}})^2 (y_i - y_{\text{aver}})^2}}$$

Cytotoxicity of ZBR Probes. The cytotoxicity of ZBR probes was evaluated by the MTT assay. Solutions of the sensors were freshly prepared in DMSO before use. HeLa cells were plated in a 96-well plate (1200 cells per well) in 200 μL of DMEM and incubated for 24 h. The cells were treated with ZBR sensors at various concentrations for an incubation period of 24 h at 37 °C, then with 20 μL of 3-(4,5-dimethylthiazol-2-yl)-2,5-diphenyltetrazolium bromide (MTT) (5 mg/mL in PBS), and incubated for 4 h. After removal of the medium, 100 μL of DMSO was added to dissolve the violet crystals, and then the absorbance of the purple formazan dye was recorded at 570 nm using a BioTek Synergy HT multi-detection microplate plate reader. For each condition, three independent experiments were carried out in triplicate. The reported percentage of cell survival values was normalized to 10 μL of DMSO 24-h-treated control cells.

Study of pH-Dependent Fluorescence. The apparent pK_a values were measured by plotting the integrated fluorescent intensity of the emission spectrum against pH recorded in the 12 to 2 range. A 5 μM (1 μM for ZBR3) solution of ZBR sensors (10 mL) containing 100 mM KCl and 1 mM EDTA was adjusted to pH 12 by KOH. The pH was adjusted in 0.5 decrements by addition of the appropriate amounts of 6, 1, 0.1, and 0.01 N HCl until reaching pH 2. The absorption and emission spectra at each pH value were recorded. The volume of the added acid was controlled so that the final change in volume was less than 1%. Emission spectra were integrated from 550 to 800 nm. The integrated emission spectral areas were normalized, plotted against pH value, and fitted to the nonlinear expression to calculate the pK_a value.

$$\Delta F = \frac{\Delta F_{1\max}}{(1 + 10^{(\text{pH}-\text{p}K_{a1})})} + \frac{\Delta F_{2\max}}{(1 + 10^{(\text{pH}-\text{p}K_{a2})})}$$

Metal Selectivity and Dissociation Constant. Metal selectivity was determined by comparing the fluorescence emission spectra of a 5.0 μM solution of the sensor in aqueous buffer at pH 7.0, before and after treatment with NaCl, $CaCl_2$, $MgCl_2$, $MnCl_2$, $FeSO_4$ (freshly prepared), $CoCl_2$, $NiCl_2$, $CuCl_2$, $CdCl_2$, or $HgCl_2$ stock solution in water, for a final cation concentration of 50 μM. Fluorescence was then recorded after subsequent addition of $ZnCl_2$ for a total concentration of 50 or 500 μM. In each case, the integrated fluorescence emission spectra were normalized with respect to the metal-free control spectrum, arbitrarily assigned as unity. The dissociation constant for Zn^{2+} of ZBR sensors was determined with Zn^{2+}/Ca^{2+}-EDTA or Zn^{2+}-EDTA buffering system, which affords concentrations of free Zn^{2+} in the nanomolar or picomolar range.[28,40] Excitation was provided at 525 nm for ZBR1, 530 nm for ZBR2, and 535 nm for ZBR3. The response was quantified by integrating the emission intensity from 550 to 800 nm and normalizing. The plot of response versus [Zn] was fitted to the equation $R = B[\text{Zn}]/(K_d + [\text{Zn}])$, where R is the integrated fluorescence response and $B = 1$ for normalized data.

RESULTS AND DISCUSSION

Probe Design and Synthesis. Previous work with functionalized fluoresceins in our laboratory has led to the development of a large number of green-emitting probes with dissociation constants covering 6 orders of magnitude, from sub-millimolar to sub-nanomolar.[27] This careful tuning was achieved by rational modification of the metal-binding group and minor alteration of the appended fluorescein platform. Seeking to develop probes that have lower energy excitation and emission wavelengths, are more amenable to live-cell imaging experiments that require prolonged observation, and are suitable for multicolor multianalyte microscopy experiments, we adopted the benzoresorufin fluorophore as the design platform. We sought to retain the $[N_3O]$ coordination motif offered by ZP and ZPP sensors (Figure 1) in order to produce probes with similar zinc-binding properties, thus allowing us to translate previous research on green fluorescein-based probes into red-emitting sensors with predictable Zn^{2+} dissociation constants. The benzophenoxazone (benzoresorufin) molecule presents an oxygen atom poised to participate in zinc binding similar to that offered by the hydroxylxanthenone core of fluorescein dyes. The general synthetic scheme for the ZBR probes is depicted in Scheme 1.

Scheme 1. Synthesis of ZBR Sensors

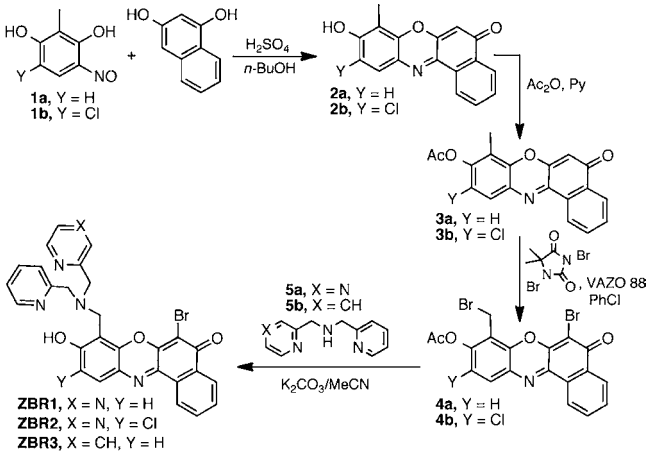

Assembly of the fluorophore starts with condensation of an appropriate 2-methyl-substituted resorcinol (**1a** or **1b**) and 1,3-dihydroxynaphthalene under acidic conditions, followed by acylation of the resulting benzoresorufin in a mixture of acetic anhydride and pyridine. This esterification step aids in the purification of the fluorophores and increases their solubility in nonpolar solvents, thus facilitating further manipulation in the subsequent steps. The acylated methyl-substituted benzoresorufins **2a** and **2b** were subjected to radical bromination conditions, resulting in the halogenation of both benzylic and quinoid positions in good yields. Occasional precipitation of the ring-brominated intermediate in the reaction mixture resulted in sluggish rates for the second, benzylic, bromination. Adjustment of the reaction temperature helped avoid this problem. With bromomethyl intermediates **4a**[36] and **4b** in hand, reaction with the appropriate picolylamine derivative **5a** or **5b** gave compounds ZBR1−3 in moderate yields. The dipicolylamine-containing analogue, ZBR3, was characterized crystallographically in its metal-free form (Figure S7 and Table S1), showing the $[N_3O]$ metal binding pocket in a geometry resembling that of ZP1.[29]

Spectroscopic Properties of ZBR Sensors. All members of the ZBR family produce light-pink and non-fluorescent solutions in either aqueous media or organic solvents, including DMSO, acetone, MeOH, and CH_3CN. Addition of zinc salts in aqueous solution or organic solvents leads to the development of a purple color and red fluorescence. Table 1 summarizes the

dx.doi.org/10.1021/ja4059487 | J. Am. Chem. Soc. 2013, 135, 13512−13520

Table 1. Spectroscopic Properties of ZBR Derivatives

	absorption[a] λ_{max} (nm), $\varepsilon \times 10^4$ (M^{-1} cm^{-1})		excitation[a] λ_{max} (nm)		emission[a] λ_{max} (nm), Φ[b]			
probe	unbound	Zn(II)-saturated	unbound	Zn(II)-saturated	unbound	Zn(II)-saturated	K_d (nM)	fluorescence pK_a
ZBR1	478, 1.93(6)	530, 2.64(1)	514	525	625, 0.067(6)	628, 0.41(3)	0.69(4)	5.35(5), 8.15(5)
ZBR2	480, 1.69(9)	524, 2.56(1)	550	530	630, 0.069(6)	630, 0.22(3)	0.70(4)	4.42(7), 7.33(4)
ZBR3	480, 1.33(4)	535, 1.93(8)	530	535	623, 0.342(7)	628, 0.60(3)	<0.001[c]	5.08(9), 8.71(8)

[a]Measurements were performed in 50 mM PIPES buffer at pH 7.0 with 100 mM KCl. [b]Resorufin (Φ_{572} = 0.74 at pH 9.5) was used as a standard for quantum yield determination. Standard deviations in the last significant digit are shown in parentheses. [c]Limited solubility of ZBR3 under the titration conditions precluded the accurate determination of the apparent K_d; an estimated upper limit is provided based on the range of $[Zn^{2+}]$ at which fluorescence saturation was observed.

spectroscopic properties of ZBR sensors determined in aqueous solution. At pH 7, all ZBR probes exhibit a very broad absorption band with maxima at 478−480 nm, as shown in Figures 2, S8, and S9. Upon zinc binding, a bathochromic shift

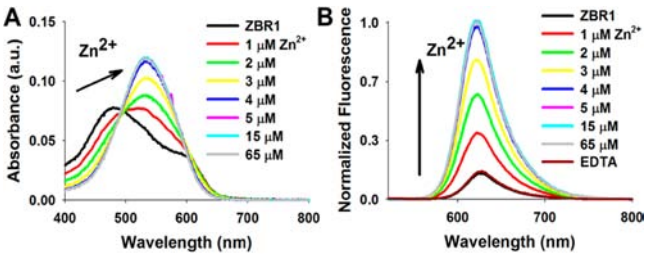

Figure 2. (A) Absorption and (B) normalized fluorescence emission spectra of ZBR1 at different total concentrations of Zn^{2+}. Spectra were acquired on 5 μM solutions of ZBR1 in 100 mM KCl, 50 mM PIPES, pH 7.0, at 25 °C, after the addition of increasing amounts of total $ZnCl_2$, followed by 100 μM EDTA. λ_{ex} = 525 nm.

in the absorption spectrum was observed in all cases. In the metal-free form, the fluorescence of the ZBR sensors is quenched, most likely due to photoinduced electron transfer from the Zn^{2+} binding unit.[36,41] Binding of Zn^{2+} induces a sharpening of the main absorption band and increases the fluorescence emission, with a Stokes shift in some cases exceeding 100 nm. Such a large Stokes shift is particularly advantageous for biological imaging experiments by fluorescence microscopy. For example, excitation of ZBR1 at 514 nm leads to a weak emission, Φ(ZBR1) = 0.067 ± 0.006, with maximum at 625 nm. Upon addition of excess Zn^{2+}, the excitation maximum shifts to 525 nm and the emission maximum to 628 nm, with a fluorescence quantum yield of Φ(ZBR1-Zn^{2+}) = 0.41 ± 0.03 for an overall 8.4-fold increase in brightness (Figure 2B). The change in the absorption and emission spectra observed upon metal binding can be reversed easily with chelators that compete with the sensor for metal coordination, such as EDTA or TPA. The apparent Zn^{2+} dissociation constants for all probes were determined by fluorescence titration employing buffered zinc systems[28,40] (Figures 3 and S12). Nonlinear fits of plots of normalized fluorescence intensity versus $[Zn^{2+}]_{free}$ rendered K_d values of 0.69 ± 0.04 nM for ZBR1 and 0.70 ± 0.04 nM for ZBR2. Both values are comparable to the apparent K_d = 0.4 nM corresponding to the second Zn^{2+} dissociation event for ZPP1, thus suggesting that the new benzoresorufin platform may be employed to produce red analogues of our green-emitting fluorescein-based sensors with predictable binding properties. The dipicolylamine derivative ZBR3 displays a zinc binding constant at least three orders of magnitude tighter than

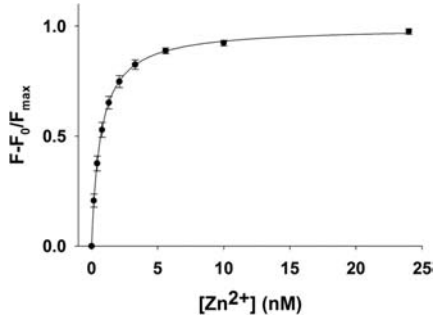

Figure 3. Integrated emission intensity of 1 μM ZBR1 vs $[Zn^{2+}]_{free}$ in aqueous buffer at 25 °C (100 mM KCl, 50 mM PIPES, pH 7.0). λ_{ex} = 525 nm.

those of the pyrazine-containing analogues ZBR1 and ZBR2, a trend that reproduces the binding of ZP1 and ZPP1 fluorescein derivatives.

The absorbance and fluorescence emission spectra of ZBR sensors are sensitive to changes in pH owing to their proton-binding properties. Under basic conditions (pH 11), ZBR1 displays strong broad absorbance between 570 and 610 nm corresponding to its fully deprotonated form (Figure 4A). At

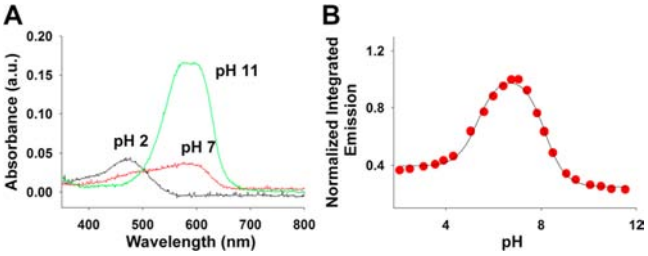

Figure 4. Effect of pH on a 5 μM solution of ZBR1 (100 mM KCl, 25 °C). (A) Representative UV−vis absorption spectra at different pH values. (B) Plot of the normalized integrated emission intensity vs pH. The pK_a values were obtained from fitting the experimental data (red circles) to a nonlinear model (continuous line).

pH 7, absorption in this wavelength range is significantly weaker. Furthermore, at acidic pH (pH 2), the broad band centered at 590 nm completely disappears and another weak absorption band appears at 490 nm. The fluorescence response of ZBR1 in the range of pH 2−12 was monitored as well (Figure 4B). The maximum emission intensity of metal-free probe was observed at pH 7. Reduced emission at high pH is most likely due to the full quenching effect of the pendant amine on the fluorophore, which in turn is abolished at neutral pH values as the amine becomes partially protonated. At acidic pH, the fluorophore itself becomes protonated and the

emission efficiency decreases, an effect previously documented for non-functionalized resorufin.[37] Nonlinear fits of the emission intensity as a function of pH afforded two apparent pK_a values: pK_{a1} = 5.35 ± 0.05 and pK_{a2} = 8.15 ± 0.05. The fitting for ZBR2 gave the pK_a values as pK_{a1} = 4.4 and pK_{a2} = 7.3 (Figure S10). The incorporation of the chloro substituent has an effect on the apparent pK_a. In particular, the first pK_a, corresponding to deprotonation of the resorufin fluorophore, is reduced by almost one unit due to the electron-withdrawing effect of the Cl atom.

The fluorescence response of the three ZBR sensors to a variety of biologically relevant metal ions was investigated. As shown in Figures 5, S13, and 14, the treatment of ZBR1 and the

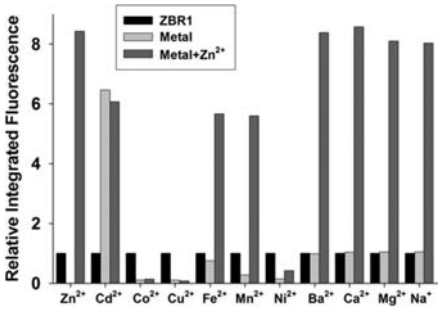

Figure 5. Metal selectivity of ZBR1 in aqueous solution at pH 7.0 (50 mM PIPES, 100 mM KCl). For each sample, 5 μM ZBR1 was treated with 50 μM metal ion of interest (light gray) and then subsequently with 50 μM $ZnCl_2$ (dark gray). The integrated fluorescence (550−800 nm) after each addition was normalized to the fluorescence of the metal-free sensor. λ_{ex} = 525 nm.

other ZBR sensors with alkali and alkaline-earth metals has no effect on the fluorescence whereas paramagnetic transition metal ions such as Mn^{2+}, Fe^{2+}, Co^{2+}, Ni^{2+} and Cu^{2+} quench the emission. Iron and manganese, however, may be displaced by zinc, leading to a partial restoration in the fluorescence.

Live Cell Imaging of ZBR Sensors. The cytotoxicity of the ZBR sensors, a critical factor to be considered for their utilization in live cell imaging, was assessed by MTT assays in HeLa cells. Figure S15 shows the cell viability data for HeLa cells treated with ZBR probes, suggesting that these cells are not damaged following a 24 h treatment with 1 μM ZBR1, ZBR2, or ZBR3. Decreased cell survival (88 ± 5%) occurred following 24 h incubation with 5 μM ZBR1, but no significant cell loss was noticed compared to the control. These results indicate that low micromolar concentrations of ZBR sensors are essentially nontoxic over at least a 24 h period and can be applied in biological studies that require lengthy sensor incubation times.

The ability of the ZBR sensor family to track zinc ions in living cells was investigated. HeLa cells (Figure 6) were incubated with 5 μM ZBR1 for 30 min at 37 °C before imaging. Because of the low level of endogenous fluorescence from the cells in the red region, in addition to the low quantum yields of the metal-free probes, there is imperceptible background signal before the addition of exogenous zinc (Figure 6D). The intracellular fluorescence increased in response to addition of exogenous zinc as the 1:2 complex Zn^{2+}/ionophore pyrithione (2-mercaptopyridine-*N*-oxide) (Figure 6E). Integration of the fluorescence signal over the cell body indicated an ∼6-fold increase when excess Zn^{2+} is present. The signal decreased substantially after treatment with 50 μM of the chelator TPA

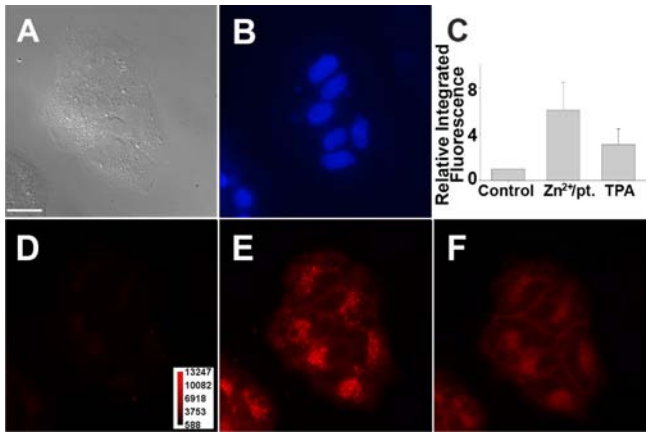

Figure 6. Fluorescence microscopy of live HeLa cells incubated with 5 μM ZBR1 and 5 μM Hoechst 33258 at 37 °C for 30 min. (A) Bright-field transmission image. (B) Nuclear staining by Hoechst 33258. (C) Quantification of Zn^{2+}-induced ZBR1 fluorescence response. (D) ZBR1 fluorescence without addition of exogenous Zn^{2+}. (E) ZBR1 fluorescence 5 min after treatment with 25 μM Zn^{2+}/pyrithione (1:2). (F) ZBR1 fluorescence 5 min after addition of 50 μM TPA (mean ± SD, N = 22). Scale bar = 25 μm.

(Figure 6C,F). The Zn^{2+} response of ZBR2 and ZBR3 was also tested and quantified (Figures S16 and S17). These results prove that the ZBR sensor family is cell-permeable and can be efficiently used to image intracellular labile Zn^{2+} within living cells.

Because the localization of small-molecule sensors is affected by a number of factors, the subcellular localization of the ZBR sensor family was investigated in different cell lines including HeLa, RAW 246.7, and NSCs. For example, co-incubation of HeLa cells with ZBR1 and either a Hoechst 33258, MitoTracker Green, or Bac-Mam 2.0 Golgi stain (Figures 7, S18, and S23) reveals that ZBR1 does not localize significantly to either the nucleus, mitochondria, or Golgi apparatus (Pearson's correlation coefficients of 0.002, 0.165, and 0.072 respectively). On the other hand, good overlap of ER-Tracker

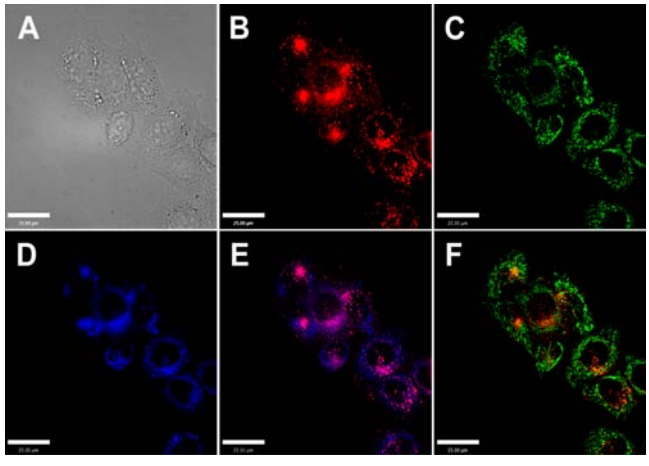

Figure 7. Co-localization analysis of ZBR1 with organelle-specific markers in HeLa cells incubated with 5 μM ZBR1, 1 μM ER-Tracker, and 0.2 μM MitoTracker Green for 30 min, and then treated with 25 μM Zn^{2+}/pyrithione (1:2) on the microscope stage. (A) Bright-field image. (B) ZBR1. (C) MitoTracker Green. (D) ER-Tracker. (E) Overlay of ZBR1 and ER-Tracker. (F) Overlay of ZBR1 and MitoTracker Green. Scale bar = 25 μm.

dx.doi.org/10.1021/ja4059487 | J. Am. Chem. Soc. 2013, 135, 13512−13520

and ZBR1 was observed in HeLa, RAW 246.7 cells, and NSCs (Figures 7, S19, S20, and S23). The Pearson's correlation coefficient values were 0.652, 0.575, and 0.699 for the respective co-localizations.

To confirm the spatial localization of ZBR1, 3D images were reconstructed from images obtained at different values along the *Z*-axis. The 3D images of NSCs clearly indicate true co-localization of ZBR1 and ER as opposed to the artifact of organelle overlap when projected down the *Z*-axis (Figure 8).

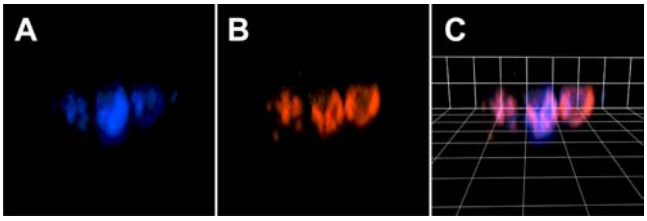

Figure 8. 3D representations of co-localization analysis within NSCs. (A) ER-Tracker fluorescence. (B) ZBR1 fluorescence. (C) Overlay of ZBR1 and ER-Tracker fluorescence. See Figure S20 for 2D images of NSCs. Scale grid = 13 μm.

The other ZBR sensors similarly display good co-localization with ER stains in the tested cell lines (Figures S21 and S22). Although ZBR1 had moderate to strong co-localization with ER-Tracker in three cell lines, the subcellular localization of small-molecule sensors is adventitious, and the accumulation of ZBRs in the ER must be confirmed for each cell line. Nonetheless, the ability of the ZBR sensors to spontaneously accumulate at specific subcellular locales renders them valuable tools for the study of labile zinc trafficking between the cytoplasm and cellular organelles.

Peroxynitrite-Induced Released Labile Zn^{2+} in the ER. Previous studies have shown that peroxynitrite induces ER stress and triggers the release of labile Zn^{2+} from intracellular stores in neuronal cells.[12,42] The source of released labile Zn^{2+}, however, is still under debate owing to the lack of readily applicable organelle-specific sensors for this ion. With our new ER-specific fluorescent probes for labile Zn^{2+} in hand, we sought to investigate further the interplay between peroxynitrite and Zn^{2+} homeostasis in the ER of NSCs and evaluate the ER as a possible source of the released Zn^{2+}.

Fluorescence imaging of NSCs treated with ZBR1 showed accumulation of endogenous Zn^{2+} in the ER without the addition of external ionophores. The growth media for NSCs contains 2 μM total Zn^{2+} (information supplied by GIBCO and confirmed by independent measurements in our laboratory). The use of Zn^{2+}-depleted preparations as growth medium (e.g., DMEM, with an estimated Zn^{2+} concentration in the nM range) led to a significantly lower ER-localized signal. We treated the cells with 3-morpholinosydnonimine (Sin-1), a reagent that releases NO and superoxide simultaneously at physiological pH,[43] which results in the generation of peroxynitrite *in situ* with a half-life of 14−26 min in common buffers.[44] Images of Zn^{2+}-induced ZBR1 fluorescence in NSCs at different time periods after the addition of 100 μM Sin-1 revealed a loss of signal intensity, consistent with zinc release. As indicated in Figures 9 and 10, in the first 15 min after addition of peroxynitrite there is a statistically significant decrease in the fluorescence intensity of ZBR1 compared to treatment with vehicle (PBS) over the same time period (89 ± 4% versus 105 ± 7%, Figure 10). The time scale of the observed changes is consistent with the kinetics of decomposition of Sin-1, thus indicating a rapid effect of the reactive species on the Zn^{2+} levels within the ER. Exogenous Zn^{2+}/pyrithione (1:2) followed by TPA was applied at the end of the experiments to confirm that ZBR1 is still localized in the cells and that the change of fluorescence intensity is indeed produced by a decrease in labile Zn^{2+} and not by diffusion of the dye out of the organelle, photobleaching, or loss of cell viability. To rule out direct interaction between Sin-1 and ZBR1 or the sensor-Zn^{2+} complex, the effect of Sin-1 on the absorption and emission spectra of ZBR1 in its metal-free and -bound form was tested in the cuvette. The results showed

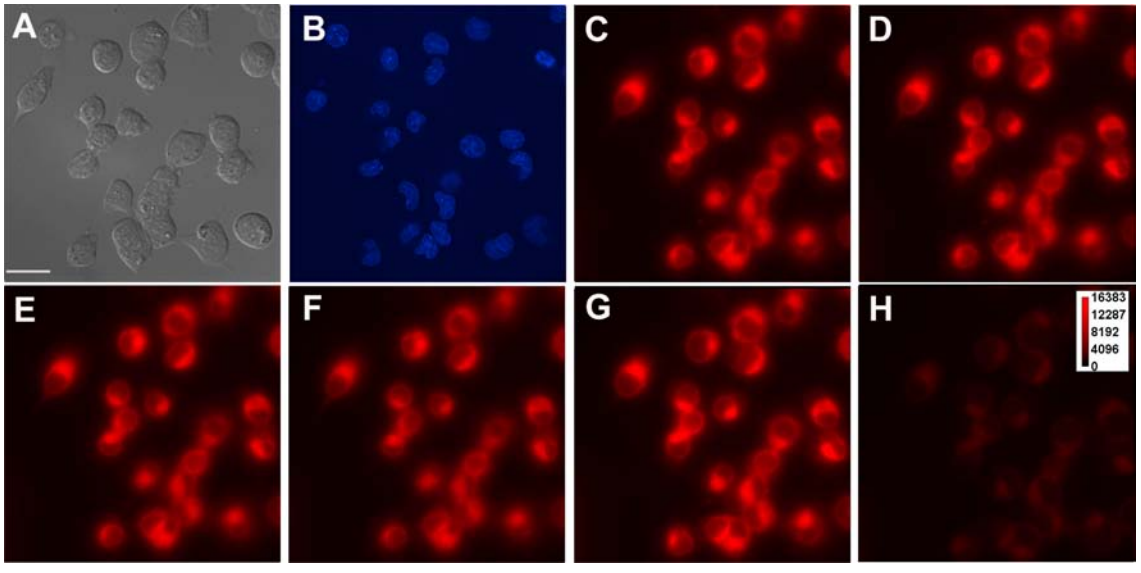

Figure 9. Representative images of Sin-1-induced ZBR1 fluorescence change in NSCs. (A) Bright-field image of NSCs. (B) Nuclear staining by Hoechst 33258. (C−H) Fluorescence images of ZBR1 (C) before the addition of 100 μM Sin-1, (D) 5 min after the addition of Sin-1, (E) 10 min after the addition of Sin-1, (F) 15 min after the addition of Sin-1, (G) 5 min after the addition of 25 μM Zn^{2+}/pyrithione (1:2), and (H) 5 min after the addition of 50 μM TPA. Scale bar = 25 μm.

dx.doi.org/10.1021/ja4059487 | *J. Am. Chem. Soc.* 2013, 135, 13512−13520

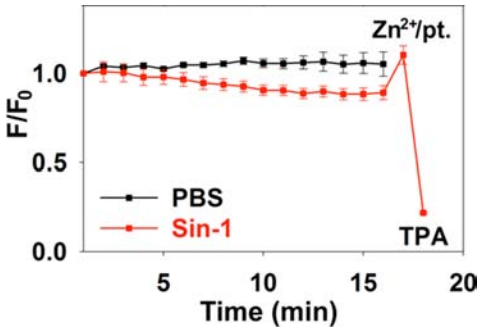

Figure 10. Quantification of Sin-1-induced ZBR1 fluorescence change in NSCs over the course of 15 min. Images (100-ms exposure) were taken before and every minute after the addition of 100 μM Sin-1 (red squares) or phosphate-buffered saline (PBS), the vehicle for Sin-1 (black squares). After 15 min, samples were treated with 25 μM Zn^{2+}/pyrithione (1:2) followed by 50 μM TPA ($N \geq 12$; mean ± SEM).

that 100 μM Sin-1 has no significant effect on the emission of ZBR1 or the sensor-Zn^{2+} complex (Figure S24). Taken together, these results suggest that the decrease in fluorescence intensity from ZBR1 is due to the mobilization of zinc from the ER in response to RNS-induced stress.

SUMMARY AND CONCLUSIONS

We prepared and characterized a new family of red-emitting fluorescent sensors for mobile Zn^{2+} based on a benzoresorufin fluorophore functionalized with pyridine- and pyrazine-containing metal binding groups. The new probes, with a conserved $[N_3O]$ metal binding motif, have apparent binding affinities comparable to those measured for fluorescein-based counterparts ZPP1 and ZP1, which contain similar binding groups. These results indicate that the benzoresorufin platform can serve as the basis for the design of new red-emitting sensors with predictable binding properties, based upon simple extrapolation of trends in coordinating properties observed for hydroxy-xanthenone-containing probes such as fluorescein-based sensors. The sub-nanomolar dissociation constant of ZBR1 and ZBR2 makes them suitable for detecting changes in intracellular labile Zn^{2+} with little background interference. The new ZBR sensors spontaneously localize in the ER of various tested cell lines and make them valuable for the investigation of zinc trafficking into and out of this organelle. This property confers them with the potential utility for investigating zinc in ER stress and various related phenomena such as unfolded protein response. We provide direct observation of the depletion of labile zinc induced by peroxynitrite in the ER of neural stem cells. Further studies will be aimed at characterizing the destination of released Zn^{2+} under ER stress and the possible downstream signaling pathways thereby triggered.

ASSOCIATED CONTENT

Supporting Information

X-ray crystallographic data in CIF format, NMR spectroscopic data, absorption and emission profiles, pH profiles, metal selectivity plots, cytotoxicity data, images of Zn^{2+}-induced response of all probes, co-localization studies in RAW 246.7 cells and NSCs, and absorption and emission profiles of the probes in the presence of Sin-1. This material is available free of charge via the Internet at http://pubs.acs.org.

AUTHOR INFORMATION

Corresponding Author

lippard@mit.edu

Notes

The authors declare no competing financial interest.

ACKNOWLEDGMENTS

This work was supported by NIH grant GM065519 from the National Institute of General Medical Sciences. Spectroscopic instrumentation in the MIT DCIF is maintained with funding from 1S10RR13886-01. We thank Prof. Fred Gage from the Salk Institute, San Diego, for a generous donation of NSCs and Dr. Andrei Loas for insightful discussions.

REFERENCES

(1) Vallee, B. L.; Auld, D. S. *Biochemistry* **1990**, *29*, 5647.
(2) Takeda, A. *Brain Res. Rev.* **2000**, *34*, 137.
(3) Vallee, B. L.; Auld, D. S. *Acc. Chem. Res.* **1993**, *26*, 543.
(4) Andreini, C.; Banci, L.; Bertini, I.; Rosato, A. *J. Proteome Res.* **2005**, *5*, 196.
(5) Dupont, C. L.; Yang, S.; Palenik, B.; Bourne, P. E. *Proc. Natl. Acad. Sci. U.S.A.* **2006**, *103*, 17822.
(6) Eide, D. J. *Biochim. Biophys. Acta* **2006**, *1763*, 711.
(7) Maret, W.; Krezel, A. *Mol. Med.* **2007**, *13*, 371.
(8) Beyersmann, D.; Haase, H. *Biometals* **2001**, *14*, 331.
(9) Haase, H.; Rink, L. *Annu. Rev. Nutr.* **2009**, *29*, 133.
(10) Fukada, T.; Yamasaki, S.; Nishida, K.; Murakami, M.; Hirano, T. *J. Biol. Inorg. Chem.* **2011**, *16*, 1123.
(11) Lin, W.; Mohandas, B.; Fontaine, C.; Colvin, R. *Biometals* **2007**, *20*, 891.
(12) Bossy-Wetzel, E.; Talantova, M. V.; Lee, W. D.; Scholzke, M. N.; Harrop, A.; Mathews, E.; Gotz, T.; Han, J.; Ellisman, M. H.; Perkins, G. A.; Lipton, S. A. *Neuron* **2004**, *41*, 351.
(13) Zhang, Y.; Wang, H.; Li, J.; Jimenez, D. A.; Levitan, E. S.; Aizenman, E.; Rosenberg, P. A. *J. Neurosci.* **2004**, *24*, 10616.
(14) Tong, L.; Heim, R. A.; Wu, S. *Free Radical Biol. Med.* **2011**, *50*, 1717.
(15) Uehara, T.; Nakamura, T.; Yao, D.; Shi, Z.-Q.; Gu, Z.; Ma, Y.; Masliah, E.; Nomura, Y.; Lipton, S. A. *Nature* **2006**, *441*, 513.
(16) Hoozemans, J. J. M.; Scheper, W. *Int. J. Biochem. Cell Biol.* **2012**, *44*, 1295.
(17) Jeong, J.; Walker, J. M.; Wang, F.; Park, J. G.; Palmer, A. E.; Giunta, C.; Rohrbach, M.; Steinmann, B.; Eide, D. J. *Proc. Natl. Acad. Sci. U.S.A.* **2012**, *109*, E3530.
(18) Ellis, C. D.; MacDiarmid, C. W.; Eide, D. J. *J. Biol. Chem.* **2005**, *280*, 28811.
(19) Wang, M.; Xu, Q.; Yuan, M. *Plant Signaling Behav.* **2011**, *6*, 77.
(20) Song, H. J.; Stevens, C. F.; Gage, F. H. *Nat. Neurosci.* **2002**, *5*, 438.
(21) Yao, J.; Mu, Y. L.; Gage, F. H. *Protein Cell* **2012**, *3*, 251.
(22) Brennand, K. J.; Gage, F. H. *Stem Cells* **2011**, *29*, 1915.
(23) Pan, E.; Zhang, X.-a.; Huang, Z.; Krezel, A.; Zhao, M.; Tinberg, C. E.; Lippard, S. J.; McNamara, J. O. *Neuron* **2011**, *71*, 1116.
(24) Sensi, S. L.; Paoletti, P.; Koh, J.-Y.; Aizenman, E.; Bush, A. I.; Hershfinkel, M. *J. Neurosci.* **2011**, *31*, 16076.
(25) Huang, Y. Z.; McNamara, J. O. *J. Neurosci.* **2012**, *32*, 15521.
(26) Takeda, A.; Tamano, H. *Metallomics* **2012**, *4*, 614.
(27) Nolan, E. M.; Lippard, S. J. *Acc. Chem. Res.* **2008**, *42*, 193.
(28) Walkup, G. K.; Burdette, S. C.; Lippard, S. J.; Tsien, R. Y. *J. Am. Chem. Soc.* **2000**, *122*, 5644.
(29) Wong, B. A.; Friedle, S.; Lippard, S. J. *J. Am. Chem. Soc.* **2009**, *131*, 7142.
(30) Buccella, D.; Horowitz, J. A.; Lippard, S. J. *J. Am. Chem. Soc.* **2011**, *133*, 4101.
(31) Chang, C. J.; Nolan, E. M.; Jaworski, J.; Burdette, S. C.; Sheng, M.; Lippard, S. J. *Chem. Biol.* **2004**, *11*, 203.

(32) Nolan, E. M.; Ryu, J. W.; Jaworski, J.; Feazell, R. P.; Sheng, M.; Lippard, S. J. *J. Am. Chem. Soc.* **2006**, *128*, 15517.
(33) Zhang, X.-a.; Hayes, D.; Smith, S. J.; Friedle, S.; Lippard, S. J. *J. Am. Chem. Soc.* **2008**, *130*, 15788.
(34) Ghosh, S. K.; Kim, P.; Zhang, X.-a.; Yun, S.-H.; Moore, A.; Lippard, S. J.; Medarova, Z. *Cancer Res.* **2010**, *70*, 6119.
(35) Lukhtanov, E. A.; Vorobiev, A. V. *J. Org. Chem.* **2008**, *73*, 2424.
(36) Apfel, U.-P.; Buccella, D.; Wilson, J. J.; Lippard, S. J. *Inorg. Chem.* **2013**, *52*, 3285.
(37) Bueno, C.; Villegas, M. L.; Bertolotti, S. G.; Previtali, C. M.; Neumann, M. G.; Encinas, M. V. *Photochem. Photobiol.* **2002**, *76*, 385.
(38) Palmer, T. D.; Takahashi, J.; Gage, F. H. *Mol. Cell. Neurosci.* **1997**, *8*, 389.
(39) Takahashi, J.; Palmer, T. D.; Gage, F. H. *J. Neurobiol.* **1999**, *38*, 65.
(40) Vinkenborg, J. L.; Nicolson, T. J.; Bellomo, E. A.; Koay, M. S.; Rutter, G. A.; Merkx, M. *Nat. Methods* **2009**, *6*, 737.
(41) Kowalczyk, T.; Lin, Z.; Voorhis, T. V. *J. Phys. Chem. A* **2010**, *114*, 10427.
(42) Zhang, Y.; Wang, H.; Li, J.; Dong, L.; Xu, P.; Chen, W.; Neve, R. L.; Volpe, J. J.; Rosenberg, P. A. *J. Biol. Chem.* **2006**, *281*, 9460.
(43) Feelisch, M.; Ostrowski, J.; Noack, E. *J. Cardiovasc. Pharmacol.* **1989**, *14*, S13.
(44) Martin-Romero, F.; Gutierrez-Martin, Y.; Henao, F.; Gutierrez-Merino, C. *J. Fluoresc.* **2004**, *14*, 17.